Journal of Metals, Materials and Minerals, 35(3), e2233, 2025

Facile synthesis of $BaMnO_3$-ZrO_2 composite: A step towards the photocatalytic degradation of organic dye

Kirttimayee MOHANTA[1], Swayam Aryam BEHERA[1], Binita NANDA[1], P. Ganga Raju ACHARY[1,*]

[1] *Department of Chemistry, Faculty of Engineering and Technology (ITER), Siksha 'O' Anusandhan (Deemed to be University), Bhubaneswar, India*

***Corresponding author e-mail**: pgrachary@soa.ac.in

Received date:
18 December 2024
Revised date:
7 May 2025
Accepted date:
24 May 2025

Keywords:
Methylene Blue;
Photodegradation;
$BaMnO_3$;
ZrO_2;
Photocatalyst

Abstract

Environmental contamination by synthetic dyes, particularly Methylene Blue (MB), presents a significant threat to aquatic ecosystems and human health due to their chemical stability and toxicity. This study investigates the photocatalytic degradation of MB using a $BaMnO_3$:ZrO_2 composite synthesized in a 1:2 ratio via a straightforward wet-chemical method. Structural and optical characterizations were performed using X-ray diffraction (XRD), Scanning electron microscopy (SEM), Fourier-transform infrared spectroscopy (FTIR), and Ultraviolet-visible diffuse reflectance spectroscopy (UV-DRS). The composite exhibited a reduced bandgap of 2.88 eV and uniform nanoscale morphology, both favorable for visible-light-driven photocatalysis. Under visible-light irradiation, the catalyst achieved 89% degradation efficiency within 105 min at neutral pH (7.5). These results underscore the synergistic effect of the $BaMnO_3$–ZrO_2, which facilitates effective charge separation and reactive species generation. This work highlights the composite's potential as a sustainable and reusable photocatalyst for wastewater treatment applications.

1. Introduction

Environmental pollution, particularly from industrial discharges containing synthetic dyes, poses a significant threat to aquatic ecosystems and human health [1-3]. Methylene Blue (MB), a commonly used dye in textiles and other industries, is known for its persistence in the environment and toxic effects on marine life and humans [4,5]. The challenges associated with conventional wastewater treatment methods underscore the need for innovative and efficient strategies to degrade such pollutants [6,7].

Photocatalytic degradation has emerged as a promising approach for addressing dye pollution [8,9], utilizing light-activated catalysts to facilitate the breakdown of organic contaminants into non-toxic byproducts. This process harnesses the energy of photons to generate reactive species, such as hydroxyl radicals, which can effectively degrade complex organic molecules [10,11]. Among various photocatalytic materials, perovskite-type oxides, particularly $BaMnO_3$ and ZrO_2, have gained attention due to their unique structural properties and enhanced photocatalytic activity.

In this study, the photocatalytic degradation of MB was investigated using a composite catalyst, $BaMnO_3$:ZrO_2, synthesized in a 1:2 ratio via a simple wet-chemical method. The rationale behind this specific ratio lies in the synergistic effects of barium manganese oxide and zirconium dioxide, which enhance the catalyst's photocatalytic performance. This ratio was chosen based on literature trends and our own comparative tests with 1:1 and 1:3 compositions. The 1:2 ratio provided the best surface contact and visible-light response.

Compared to the individual oxides, the $BaMnO_3$:ZrO_2 composite demonstrated superior performance due to the formation of a heterojunction interface that facilitates more efficient separation of photo-generated electron–hole pairs. While $BaMnO_3$ offers good light absorption, it suffers from rapid charge recombination; ZrO_2, on the other hand, is chemically stable but has a wide bandgap that limits visible-light activity. By combining the two, the composite benefits from enhanced light absorption, reduced bandgap, and improved charge carrier mobility, all of which contribute to significantly higher photocatalytic efficiency.

2. Experimental method

2.1 Synthesis of $BaMnO_3$

The synthesis of $BaMnO_3$ was achieved using a sol-gel method [12,13]. Initially, barium acetate ($Ba(CH_3COO)_2$) and manganese acetate ($Mn(CH_3COO)_2$) were dissolved in a stoichiometric amount of distilled water to form a homogeneous solution. The solution was heated gradually to 80°C under continuous stirring to facilitate the evaporation of water. As the solution concentrated, a gel-like precursor formed. This gel was further dried at 120°C for several hours to remove residual moisture and then calcined at 800°C for 4 h in a furnace to obtain the crystalline phase of $BaMnO_3$. The resulting powder was then cooled to room temperature and ground to a fine consistency.

2.2 Preparation of $BaMnO_3$:ZrO_2

To prepare the $BaMnO_3$:ZrO_2 composite in a 1:2 ratio, zirconium dioxide (ZrO_2) powder was used as the secondary component. The stoichiometric amounts of the previously synthesized $BaMnO_3$ and

ZrO_2 were carefully measured. The two powders were then thoroughly mixed using a mortar and pestle to ensure a homogeneous distribution of the components. The mixture was subjected to further grinding for approximately 30 minutes to enhance particle interaction and homogeneity. Subsequently, the blended powder was compacted and calcined at 800°C for 3 h. After cooling, the final product was ground to a fine powder and further characterization was performed.

2.3 Photocatalytic experiment

The photocatalytic activity of the synthesized catalysts against MB was evaluated under sunlight exposure. A 0.02 g sample of the photocatalyst was added to 20 mL of MB solution (20 ppm) and stirred in the dark for 30 min to establish adsorption-desorption equilibrium. Following this, the solution was exposed to sunlight for 105 min, under a light intensity of 100,000 lx (approximately 1200 W·m^{-2}), in Bhubaneswar, Odisha, between 12 A.M. and 2 P.M. After the exposure period, the catalyst was removed by filtration, and the filtrate was analyzed using a UV spectrophotometer (Systronics-2022) to determine the absorbance at the maximum peak of 475 nm. The photocatalytic efficiency of the catalyst was calculated using the following equation (1):

$$\eta = \left(\frac{C_0 - C}{C_0}\right) \times 100 \quad (1)$$

Where η represents the degradation percentage, C_0 is the initial concentration of the MB and C is the final concentration of MB after the reaction.

3. Results and discussion

3.1 XRD

The XRD pattern of the prepared $BaMnO_3$:ZrO_2 is showed in Figure 1(a). The XRD patterns were obtained a long monochromatic radiation (10°≤ 2θ ≤ 80°). The diffraction peaks at 2θ values of 25.80 (101), 31.37 (110), 41.06 (201), 41.70 (102), 52.57 (211), 53.09 (202), 55.83 (300), 62.97 (212), and 65.45 (220) were perfectly matched with $BaMnO_3$ of hexagonal symmetry (Space group: P63/mmc), having the cell parameters or lattice constants a=b=5.6990Å and c=4.8170Å (α=β=900 and γ=120°) (JCPDS ID: 00-026-0168) [14-16]. The diffraction peaks at 2θ values (in degrees) of 30.12 (111), 34.96 (200), 50.22 (220) and 59.74 (311) were perfectly matched with ZrO_2 of cubic symmetry (Fm-3m), having the cell parameters or lattice constants a=b=c=5.1280Å (α= β=γ=90°) (JCPDS ID: 00-049-1642) [17]. The slight broadening of diffraction peaks observed in the XRD pattern suggests potential lattice strain at the $BaMnO_3$-ZrO_2 interface, which may arise due to the ionic size mismatch between Ba^{2+}/Mn^{4+} and Zr^{4+} ions. This interfacial strain can influence crystal growth and defect formation, potentially contributing to enhanced photocatalytic activity by facilitating charge separation at the heterojunction boundary.

3.2 FTIR

The FTIR spectra of $BaMnO_3$:ZrO_2 is displayed in Figure 1(b). The stretching vibration of the –OH group of the water molecule adsorbed on the surface of $BaMnO_3$:ZrO_2. This is responsible for the strong absorption band, shown in the region of 3800 cm^{-1} to 3200 cm^{-1}, and the peak at 1632 cm^{-1} indicate the typical bending vibration of –OH group of the water molecule [18].The stretching vibration of hydroxyl zirconium (Zr–OH) bond is shown by the peak at 2360 cm^{-1} [19]. Other than that, a broad bending peak at 1400 cm^{-1} indicate the carboxylic group. The peak at 1058 cm^{-1} suggest C-O stretching and bending vibration due to primary alcohol. The peak shows at 691 cm^{-1} confirms the formation of Zr–O bond. Because of high presence of OH group at catalyst surface, it enhances photocatalytic activity of powder sample.

3.3 SEM

The surface morphology and particle characteristics of the $BaMnO_3$:ZrO_2 (1:2) composite were investigated using a ZEISS EVO-18 scanning electron microscope. Figure 2. shows SEM micrographs captured at different magnifications, providing insight into the surface features and particle distribution of the synthesized material. All images include clearly labeled scale bars for accurate size estimation. The SEM images reveal that the particles are mostly granular and aggregated with moderately uniform distribution. No significant porosity or cracking was observed, suggesting that the composite has good physical integrity after calcination. The granular morphology is conducive to enhanced light scattering and multiple photon interactions, which may improve photocatalytic efficiency.

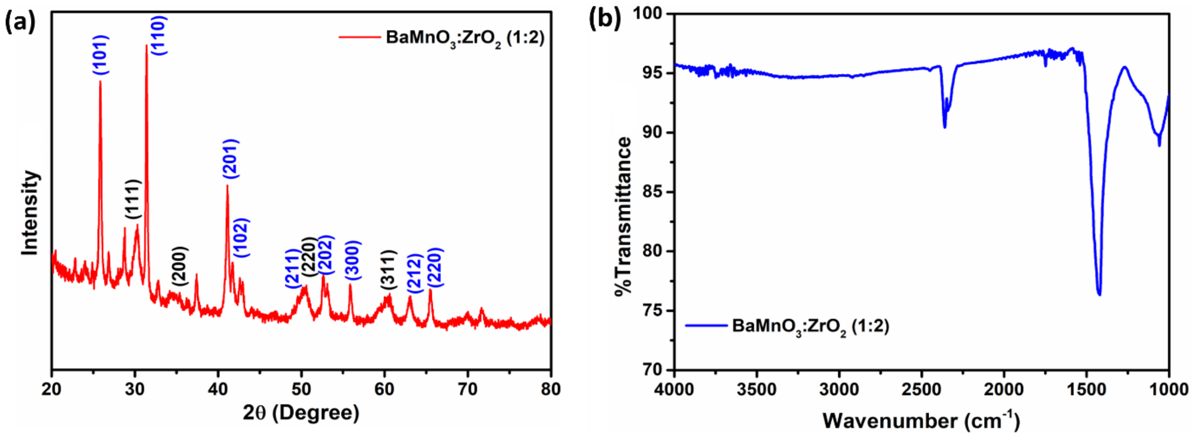

Figure 1. (a) XRD, and (b) FTIR of $BaMnO_3$:ZrO_2.

To further quantify the microstructural data, a particle size distribution curve was plotted using ImageJ software based on SEM images. The majority of particles fall within the 100 nm to 250 nm size range, with an average particle diameter of approximately 160 nm. This nanoscale size is favorable for increased surface area and better interaction with dye molecules during photocatalysis. This comprehensive analysis confirms the suitability of $BaMnO_3$:ZrO_2 morphology for photocatalytic applications, offering a good balance between surface area, particle uniformity, and material stability.

3.4 UV-DRS

The energy band gap structure is a key factor in assessing the photocatalytic activity of semiconductors [20]. To determine the energy band gap, Tauc's plot was employed, as described by the Equation (2):

$$(\alpha h\upsilon)^{1/m} = A(h\upsilon - E_g) \quad (2)$$

where h is Planck's constant, v is the incoming light frequency, α is the absorption coefficient, E_g is the band gap energy, and C is a constant. The band gap energy of the photocatalysts can be determined by plotting $(\alpha h\nu)^{1/2}$ for indirect transitions against $h\nu$. The optical absorption analysis was performed at room temperature over the 250 nm to 750 nm wavelength range, revealing a distinct peak at approximately 390 nm (Figure 3(a)), indicative of a characteristic feature in the synthesized material. The energy band gap of $BaMnO_3$:ZrO_2, which lies in the UV range, is suitable for UV-DRS analysis. The linear fit in the analysis (Figure 3(b)) allows for determining the energy band gap, with E_g for $BaMnO_3$:ZrO_2 found to be 2.88 eV, as indicated by the X-axis intercept. The composite material with an indirect bandgap of 2.88 eV exhibits enhanced visible-light absorption compared to its pure components, hexagonal $BaMnO_3$ and cubic ZrO_2.

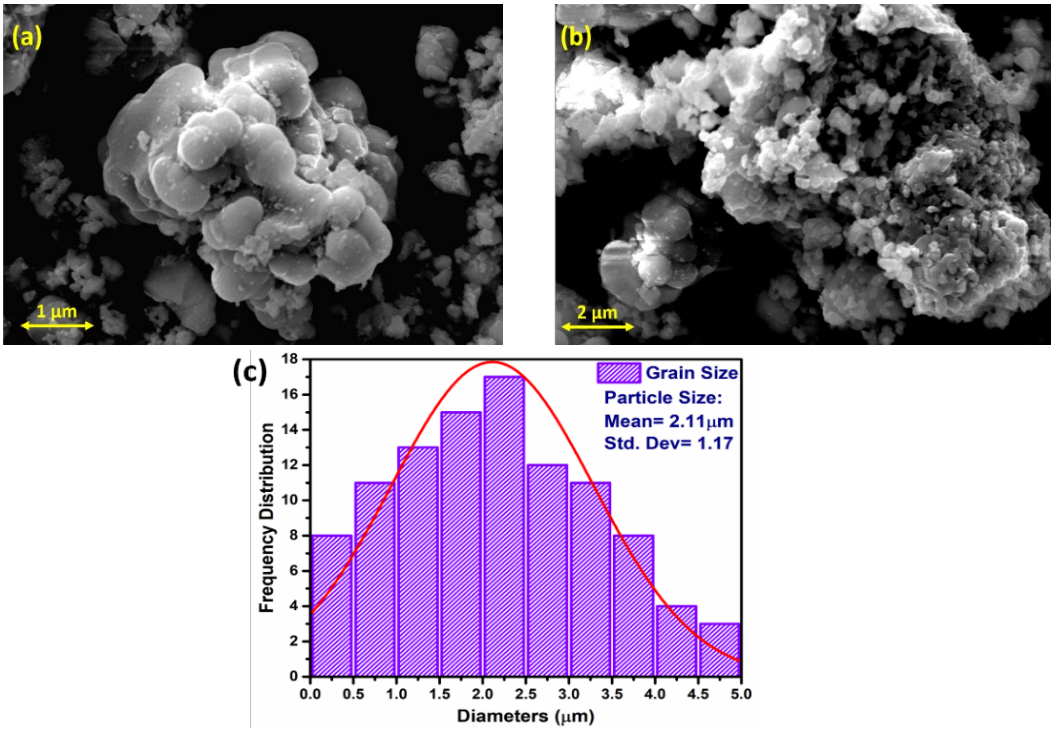

Figure 2. SEM images at different magnification and particle size distribution curve of $BaMnO_3$:ZrO_2.

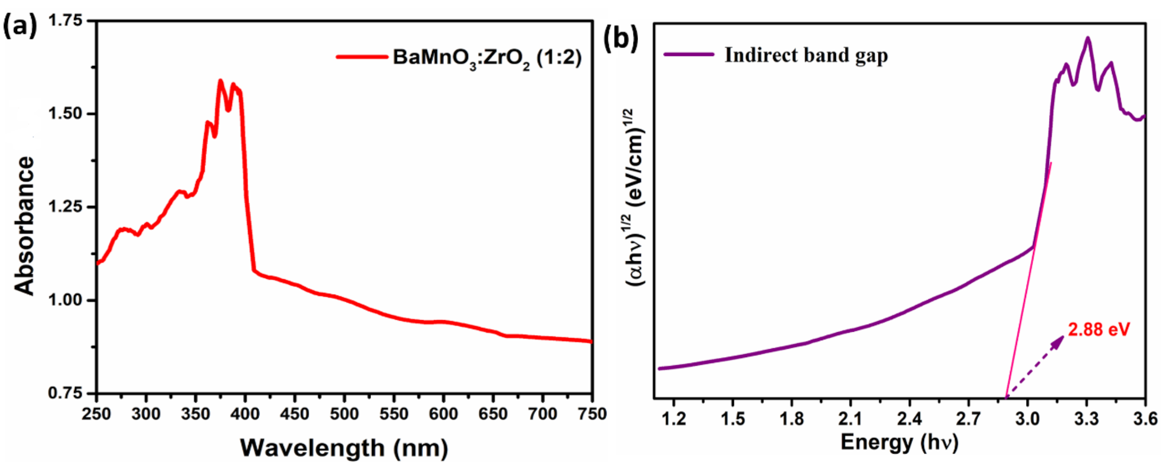

Figure 3. (a) UV-VIS-DRS absorbance spectra, & (b) Indirect bandgap of $BaMnO_3$:ZrO_2

Hexagonal $BaMnO_3$ has a bandgap of 3.2 eV [21], making it an effective antiferromagnetic semiconductor, while cubic ZrO_2 possesses a bandgap of ~4.9 eV [22], which is slightly lower than its monoclinic counterpart but still restrictive for visible-light-driven processes. The formation of the composite reduces the bandgap, facilitating improved charge carrier dynamics and enhanced light absorption, which is essential for applications such as photocatalysis and optoelectronic devices.

3.5 Photocatalytic degradation of methylene blue

The photocatalytic degradation of MB using $BaMnO_3$:ZrO_2 (1:2) was conducted to assess its efficiency. Initially, the catalyst was kept in the dark to establish adsorption-desorption equilibrium before being exposed to visible light for 105 min under a light intensity of 100,000 lx (approximately 1200 $W\cdot m^{-2}$), in Bhubaneswar, Odisha, between 12 A.M. and 2 P.M. [23]. The adsorption percentage was low (~4% to 6%), because the photocatalyst ($BaMnO_3$:ZrO_2) was not designed primarily for adsorption-based removal of MB, but rather for photocatalytic degradation under light irradiation. The reaction was monitored at 15 min intervals, with absorbance measured at 475 nm. As the reaction progressed from 15 min to 105 min, a progressive decrease in the peak intensity was observed, indicating enhanced MB degradation, as illustrated in Figure 4(a).

The pH of the solution significantly influenced the photocatalytic performance. Experiments were conducted across a range of pH values (3.5, 5.5, 7.5, and 9.5). The results demonstrated that the degradation efficiency was highest at pH 7.5 (Figure 4(b)). In contrast, an increase in pH beyond this point resulted in a decrease in degradation efficiency. This reduction can be attributed to the diminishing availability of reactive species and changes in the charge characteristics of the catalyst and MB, which affect the adsorption and subsequent degradation process.

The rate of photodegradation of MB was observed to decrease as the concentration of MB increased. This trend aligns with first-order kinetics, as described by the Equation (3):

$$\text{Log } C/C_0 = k_t \qquad (3)$$

In this equation, C represents the concentration of MB after degradation, C_0 is the initial concentration, and k is the rate constant for the reaction. The evaluation of photodegradation using $BaMnO_3$:ZrO_2 (1:2) photocatalyst is illustrated in Figure 4(c). The results indicated that as the MB concentration increased from 20 $mg\cdot L^{-1}$ to 80 $mg\cdot L^{-1}$, the photodegradation efficiency decreased. This reduction can be attributed to factors such as saturation of the catalyst's active sites and increased light scattering, which hinder the effective interaction between the photocatalyst and the dye molecules, ultimately leading to lower degradation rates.

A dose-dependent experiment was conducted under the same reaction time (105 min), at pH 7.5 using a 20 ppm MB solution, testing catalyst amounts of 0.01 g, 0.02 g, 0.04 g, 0.06 g, 1.0 g, and 1.2 g. The maximum removal efficiency of MB reached 89% at a catalyst dose of 0.02 g (Figure 4(d)). This optimal efficiency can be attributed to an ideal balance between the active sites available on the catalyst and the amount of MB in solution, allowing for effective interaction and photodegradation. As the catalyst dose increased beyond 0.02 g, the interaction between the catalyst and the dye initially improved but subsequently declined. Higher doses can obstruct light penetration and reduce the effective surface area available for the photoreaction, thereby hindering the photo-degradation of MB.

Figure 4(e) demonstrates the reduction in MB concentration over time, specifically from 15 min to 105 min. As the concentration of MB decreases, the degradation percentage correspondingly increases. This trend highlights that as the reaction continues, more of the MB dye is effectively decomposed, resulting in enhanced overall degradation efficiency. This correlation underscores the effectiveness of the photocatalytic process in breaking down the dye as time progresses.

Figure 4(f) illustrates the impact of various scavengers on the photocatalytic degradation of MB using the $BaMnO_3$:ZrO_2 composite. The rationale for selecting these specific scavengers is based on their well-established ability to selectively trap active species involved in photocatalytic reactions. Isopropanol (IP) was used as a hydroxyl radical ($^{\bullet}OH$) scavenger, para-benzoquinone (PBQ) as a superoxide radical ($^{\bullet}O_2^-$) scavenger, citric acid (CA) to trap photogenerated holes (h^+), and dimethyl sulfoxide (DMSO) to scavenge electrons (e^-). This systematic approach allows the identification of the dominant reactive species contributing to dye degradation. It can be seen that, the addition of isopropanol (IP) significantly reduced the photodegradation efficiency of MB, this would suggest that hydroxyl radicals ($^{\bullet}OH$) play a major role in the degradation process. Since hydroxyl radicals are highly reactive species often responsible for breaking down organic pollutants, their suppression would lead to a noticeable decrease in MB degradation.

To evaluate the reusability of the catalyst, it was washed with water and anhydrous ethanol after each photocatalytic experiment and subsequently dried for further use. As illustrated in Figure 4(g), the photodegradation efficiency remained largely unchanged after four consecutive cycles. This finding indicates that the catalyst $BaMnO_3$:ZrO_2 (1:2) retains its stability and effectiveness across multiple photocatalytic runs.

The photocatalytic process for degradation of MB was shown in Figure 5. Upon light irradiation, the $BaMnO_3$:ZrO_2 (1:2) composite absorbs photons and generates electron-hole (e^-/h^+) pairs. The holes (h^+) react with adsorbed water or hydroxide ions to form hydroxyl radicals ($^{\bullet}OH$), while the electrons (e^-) reduce oxygen molecules to form superoxide radicals ($^{\bullet}O_2^-$). These reactive oxygen species (ROS), especially $^{\bullet}OH$, attack the MB molecules, breaking down the dye into smaller, often non-toxic molecules or mineralized products like CO_2 and H_2O. The following reactions (Equation (4-9) occur during this photocatalytic process:

$$MB + h\upsilon \rightarrow MB\ (e^-_{CB} + h^+_{VB}) \qquad (4)$$

$$e^- + O_2 \rightarrow O_2^{-\cdot} \qquad (5)$$

$$O_2^{-\cdot} + H_2O \rightarrow HO_2^{\cdot} + OH^{\cdot} \qquad (6)$$

$$h^+ + OH^- \rightarrow OH^{\cdot}\ \text{(adsorbed)} \qquad (7)$$

$$h^+ + H_2O \rightarrow OH^{\cdot} + H^+ \qquad (8)$$

$$MB + OH^{\cdot} + O_2^{-} \rightarrow \text{Degraded products } (CO_2 \text{ and } H_2O) \qquad (9)$$

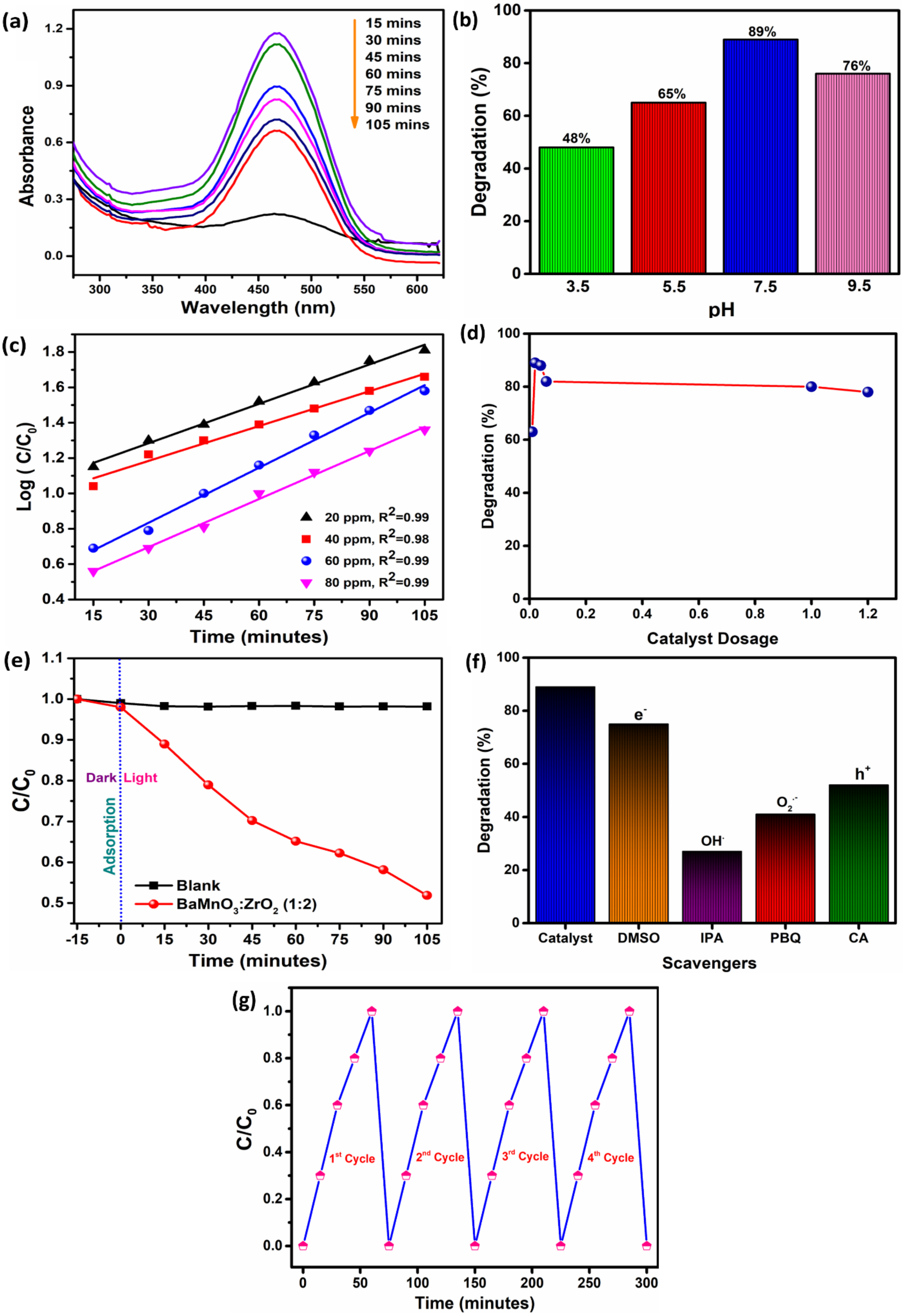

Figure 4. Photodegradation of MB by $BaMnO_3$:ZrO_2 (1:2) (a) At different time intervals, (b) At different pH, (c) Kinetics at different concentration, (d) Effect of catalyst dosage, (e) Concentration of MB over time, (f) Impact of several scavenging agents on the photodegradation process, and (g) Reusability of $BaMnO_3$:ZrO_2 (1:2).

Table 1. Recent study on different types of ZrO_2 doped photocatalyst.

Photocatalyst	Reaction Parameter	Degraded Pollutant	Efficiency	Reference
TiO_2/ZrO_2	100 W LED lamp	Rhodamine B	90%	[26]
$CuCo_2O_4@ZrO_2$	Visible light	Tetracycline	95%	[27]
g-C_3N_4/ZrO_2	50 W LED lamp, 30 mg photocatalyst	Methylene blue, Rhodamine B, Congo Red, and Tetracycline	96%, 98%, 90%, and 83%	[28]
TiO_2-ZrO_2	125 W Mercury lamp, pH = 7.6, 10 $mg \cdot L^{-1}$ photocatalyst	Metformin	92% in 150 min	[29]
ZrO_2/Dy_2O_3	Xenon lamp with cut-off UV filter	Rhodamine B, and Methylene blue	100% in 30 min and 87.79%	[30]
ZnO QDs@ZrO_2-TiO_2	Ultraviolet light	Congo Red	94.62%	[31]
RE/ZrO_2 (RE = Sm, Eu)	350 W Xenon lamp	Methylene blue and Rhodamine B	100% in 30 min and 96.3% in 90 min	[32]
Al_2O_3/ZrO_2	Visible light, 0.04 g catalyst	Reactive blue 222 and Reactive yellow 145	91.4% and 94.6% in 60 min	[33]
Nd doped ZrO_2	pH = 7	Methylene blue, Rhodamine B, and Acetophenone	90%, 77%, and 60%	[34]
C-doped ZrO_2	PL-L lamp, 0.2 $g \cdot L^{-1}$ photocatalyst	Methylene blue	75%	[35]
Ni doped ZrO_2	Visible light lamp (>400 nm), 15 mg photocatalyst	Methylene blue	90.2% in 100 min	[36]
$BaMnO_3$ doped ZrO_2	Sunlight under a light intensity of 100,000 lx, pH = 7.5	Methylene blue	89% in 105 min	Present work

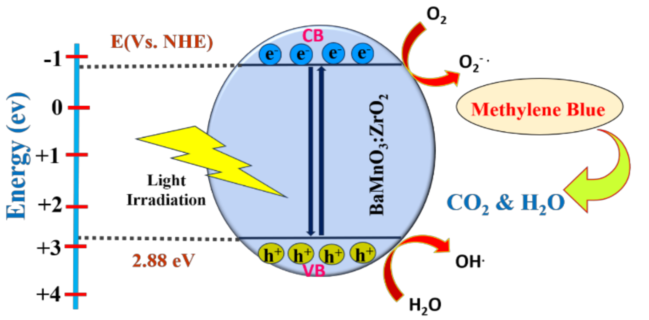

Figure 5. Photocatalytic process for degradation of MB.

The $BaMnO_3:ZrO_2$ (1:2) composite exhibits notable mechanistic advantages that contribute to its enhanced photocatalytic activity under visible-light irradiation. The formation of a heterojunction interface between $BaMnO_3$ and ZrO_2 facilitates efficient separation of photogenerated electron–hole (e^-/h^+) pairs, thereby minimizing recombination losses [24,25]. $BaMnO_3$, with its perovskite structure and moderate bandgap, enables effective light absorption, while ZrO_2 provides structural stability and acts as an electron sink due to its wide bandgap and strong electron mobility. This synergistic interaction extends the light absorption range into the visible region, improving the overall photocatalytic response. Moreover, the heterojunction promotes enhanced migration of charge carriers across the interface, increasing the likelihood of reactive oxygen species (ROS) generation, such as hydroxyl ($^{\bullet}OH$) and superoxide ($^{\bullet}O_2^-$) radicals. These mechanistic advantages collectively result in improved degradation efficiency of organic pollutants like MB. Table 1. shows a recent study on different types of ZrO_2 doped photocatalyst.

4. Conclusion

This study successfully demonstrated the photocatalytic degradation of MB using a $BaMnO_3:ZrO_2$ composite in a 1:2 ratio, synthesized via a simple wet-chemical method. The structural and optical properties of the material were confirmed using XRD, SEM, FTIR, and UV-DRS analyses. SEM micrographs revealed uniform particle morphology with an average size of approximately 160 nm, supporting a high surface-to-volume ratio beneficial for photocatalysis. The photocatalytic experiments showed an impressive degradation efficiency of 89% within 105 min under visible light at a neutral pH of 7.5. Notably, the adsorption percentage was low (~4% to 6%), indicating that MB removal was primarily due to photocatalytic activity rather than passive adsorption. This observation reinforces the material's role as a true photocatalyst rather than an adsorbent. The $BaMnO_3:ZrO_2$ enhances charge separation and light absorption, contributing to the efficient generation of reactive oxygen species (ROS), especially hydroxyl radicals ($^{\bullet}OH$), which played a dominant role in the degradation process, as confirmed by scavenger experiments. The composite displayed good recyclability over four cycles without significant loss of activity, highlighting its stability and reusability for potential large-scale wastewater treatment applications. These findings underline the practical promise of $BaMnO_3:ZrO_2$ as a robust, visible-light-responsive material for sustainable dye removal and environmental remediation.

Authorship contribution

Kirttimayee Mohanta: Formal analysis, Data curation, Writing - original draft; **Swayam Aryam Behera:** Methodology, Format analysis, Data curation, Writing - original draft; **Binita Nanda:** Supervision, Conceptualization, Review and revision; **P. Ganga Raju Achary:** Supervision, Conceptualization, Validation, Editing, Review and revision.

References

[1] H. B. Slama, A. C. Bouket, Z. Pourhassan, F. N. Alenezi, A. Silini, H. C. Sillini, T. Oszako, L. Luptakova, P. Golinska, and L Belbahri, "Diversity of synthetic dyes from textile industries, discharge impacts and treatment methods," *Applied Sciences*, vol. 11, no. 14, p. 6255, 2021.

[2] M. Yusuf, "Synthetic dyes: A threat to the environment and water ecosystem," *Textiles and Clothing*, pp. 11-26, 2019.

[3] A. Tkaczyk, K. Mitrowska, and A. Posyniak, "Synthetic organic dyes as contaminants of the aquatic environment and their implications for ecosystems: A review," *Science of the Total Environment*, vol. 717, p. 137222, 2020.

[4] P. O. Oladoye, T. O. Ajiboye, E. O. Omotola, and O. J. Oyewola, "Methylene blue dye: Toxicity and potential elimination technology from wastewater," *Results in Engineering*, vol. 16, p. 100678, 2022.

[5] O. A. Yildirim, M. Bahadir, and E. Pehlivan, "Detrimental effects of commonly used textile dyes on the aquatic environment and human health--a review," *Fresenius Environmental Bulletin*, vol. 31, pp. 9329-9345, 2022.

[6] S. A. Behera, A. Subhadarshini, S. S. Bhuyan, B. Nanda, and P. G. R. Achary, "PVDF/rGO/CuO nanocomposites: A robust platform for solar-driven tetracycline photodegradation," *Inorganic Chemistry Communications*, vol. 160, p. 111995, 2024.

[7] S. A. Behera, A. Amanat, and P. G. R. Achary, "Photocatalytic degradation of ciprofloxacin drug utilizing novel PVDF/ polyaniline/lanthanum strontium manganate@ Ag composites," *Journal of Metals, Materials and Minerals*, vol. 34, no. 1, p. 1896, 2024.

[8] S. Li, K. Rong, X. Wang, C. Shen, F. Yang, and Q. Zhang, "Design of carbon quantum dots/CdS/Ta_3N_5 S-scheme hetero-junction nanofibers for efficient photocatalytic antibiotic removal," *Acta Physico-Chimica Sinica*, vol. 40, no. 12, p. 2403005, 2024.

[9] C. You, C. Wang, M. Cai, Y. Liu, B. Zhu, and S. Li, "Improved photo-carrier transfer by an internal electric field in BiOBr/ Nrich C_3N_5 3D/2D S-scheme heterojunction for efficiently photocatalytic micropollutant removal," *Acta Physico-Chimica Sinica***,** vol. 40, no. 11, p. 2407014, 2024.

[10] L. V. Samarasinghe, S. Muthukumaran, and K. Baskaran, "Recent advances in visible light-activated photocatalysts for degradation of dyes: A comprehensive review," *Chemosphere*, p. 140818, 2023.

[11] G. Saianand, A-I. Gopalan, L. Wang, K. Venkatramanan, V. A. L. Roy, P. Sonar, D-E. Lee, and R. Naidu, "Conducting polymer based visible light photocatalytic composites for pollutant removal: Progress and prospects," *Environmental Technology & Innovation,* vol. 28, p. 102698, 2022.

[12] V. Torregrosa-Rivero, M.-S. Sánchez-Adsuar, and M.-J. Illán-Gómez, "Improving the performance of $BaMnO_3$ perovskite as soot oxidation catalyst using carbon black during sol-gel synthesis," *Nanomaterials*, vol. 12, no. 2, p. 219, 2022.

[13] V. Torregrosa-Rivero, M.-S. Sanchez-Adsuar, and M.-J. Illan-Gomez, "Analyzing the role of copper in the soot oxidation performance of BaMnO3-perovskite-based catalyst obtained by modified sol-gel synthesis," *Fuel*, vol. 328, p. 125258, 2022.

[14] K. Hayat, M. J. Iqbal, K. Rasool, and Y. Iqbal, "Device fabrication and dc electrical transport properties of barium manganite nanofibers (BMO-NFs)," *Chemical Physics Letters*, vol. 616, pp. 126-130, 2014.

[15] R. Ao, L. Ma Z. Guo, J. Yang, L. Mu, J. Yang, and Y. Wei, "NO oxidation performance and kinetics analysis of $BaMO_3$ (M= Mn, Co) perovskite catalysts," *Environmental Science and Pollution Research*, vol. 28, no. 6, pp. 6929-6940, 2021.

[16] N. Terenti, E. Me;nic, V. Fruth, N. Nedelko, P. Aleshkevych, S. Lewinska, A. Slawska-Waniewska, V. Ch. Kravtsov, A. Lazarescu, and V. Lozan, "Synthesis and microstructure of $BaMnO_3$ oxide obtained from coordination precursor," *Journal of Solid State Chemistry*, vol. 324, p. 124108, 2023.

[17] A. Kumari, K. Kumari, F. Ahmed, A. Alshoaibi, P. A. Alvi, S. Dalela, M. M. Ahmad, R. N. Aljawfi, P. Dua, A. Vij, and S. Kumar, "Influence of Sm doping on structural, ferroelectric, electrical, optical and magnetic properties of $BaTiO_3$," *Vacuum*, vol. 184, p. 109872, 2021.

[18] K. Hayat, M. A. Rafiq, and M. M. Hasan, "Synthesis and optimization of barium manganate nanofibers by electrospinning," *Ceramics International*, vol. 38, no. 2, pp. 1441-1445, 2012.

[19] N. C. Horti, M. D. Kamatagi, S. K. Nataraj, M. N. Wari, and S. R. Inamdar, "Structural and optical properties of zirconium oxide (ZrO_2) nanoparticles: Effect of calcination temperature," *Nano Express*, vol. 1, no. 1, p. 10022, 2020.

[20] S. A. Behera, D. Khatua, R. K. Singh, R. N. P. Choudhary, and P. G. R. Achary, "Temperature-dependent electrical and dielectric characteristics of lead germanate $Pb_5Ge_{1.5}Sn_{1.5}O_{11}$," *Inorganic Chemistry Communications*, vol. 163, p. 112370, 2024.

[21] T. N. Stanislavchuk, A. P. Litvinchuk, H. Rongwei, J. Y. Hun, J. S. Dae, S.-W. Cheong, and A. A. Sirenko, "Optical properties, lattice dynamics, and structural phase transition in hexagonal 2H-$BaMnO_3$ single crystals," *Physical Review B,* vol. 92, no. 13, p. 134308, 2015.

[22] D. Prakashbabu, R. H. Krishna, B. M. Nagabhushana, H. Nagabhushana, C. Shivakumara, R. P. S. Chakradar, H. B. Ramalingam, S. C. Sharma, and R. Chandramohan, "Low temperature synthesis of pure cubic ZrO_2 nanopowder: Structural and luminescence studies," *Spectrochimica Acta Part A: Molecular and Biomolecular Spectroscopy*, vol. 122, pp. 216-222, 2014.

[23] P. L. Krapivsky, and E. Ben-Naim, "Collective properties of adsorption--desorption processes," *Journal of Chemical Physics*, vol. 100, no. 9, pp. 6778-6782, 1994.

[24] S. Li, C. You, K. Rong, C. Zhuang, X. Chen, and B. Zhang, "Chemically bonded Mn0. 5Cd0.5S/BiOBr S-scheme photocatalyst with rich oxygen vacancies for improved photocatalytic decontamination performance," *Advanced Powder Materials*, vol. 3, no. 3, p. 100183, 2024.

[25] C. Shen, X. Li, B. Xue, D. Feng, Y. Liu, F. Yang, M. Zhang, and S. Li, "Surface plasmon effect combined with S-scheme charge migration in flower-like $Ag/Ag_6Si_2O_7/Bi_{12}O_{17}Cl_2$ enables efficient photocatalytic antibiotic degradation," *Applied Surface Science*, vol. 679, p. 161303, 2025.

[26] J. Abdi, M. Yahyanezhad, S. Sakhaie, M. Vossoughi, and I. Alemzadeh, "Synthesis of porous TiO_2/ZrO_2 photocatalyst derived from zirconium metal organic framework for degradation of organic pollutants under visible light irradiation," *Journal of Environmental Chemical Engineering*, vol. 7, no. 3, p. 103096, 2019.

[27] M. R. Alotaibi, and M. H. H. Mahmoud, "Promptness of tetracycline pollutant degradation via $CuCo_2O_4$@ZrO_2 nanocomposites photocatalyst," *Optical Materials (Amst).*, vol. 126, p. 112200, 2022.

[28] M. Tanzifi, M. Jahanshahi, M. Peyravi, and S. Khalili, "A morphological decoration of g-C_3N_4/ZrO_2 heterojunctions as a visible light activated photocatalyst for degradation of various organic pollutants," *Journal of Environmental Chemical Engineering*, vol. 10, no. 6, p. 108600, 2022.

[29] C. F. Carbuloni, J. E. Savoia, J. S. P. Santos, C. A. A. Pereira, R. G. Marques, V. A. S. Ribeiro, and A. M. Ferrari, "Degradation of metformin in water by TiO_2-ZrO_2 photocatalysis," *Journal of Environmental Management*, vol. 262, p. 110347, 2020.

[30] W. Du, X. Wang, H. Li, D. Ma, S. Hou, J. Zhang, X. Qian, and H. Pang, "ZrO_2/Dy_2O_3 solid solution nano-materials: tunable composition, visible light-responsive photocatalytic activities and reaction mechanism," *Journal of the American Ceramic Society*, vol. 96, no. 9, pp. 2979-2986, 2013.

[31] Q. Zhou, L. Li, X. Zhang, H. Yang, Y. Cheng, H. Che, L. Wang, and Y. Cao, "Construction of heterojunction and homojunction to improve the photocatalytic performance of ZnO quantum dots sensitization three-dimensional ordered hollow sphere ZrO_2-TiO_2 arrays," *International Journal of Hydrogen Energy*, vol. 45, no. 56, pp. 31812-31824, 2020.

[32] W. Du, Z. Zhu, X. Zhang, D. Wang, D. Liu, X. Qian, and J. Du, "RE/ZrO_2 (RE= Sm, Eu) composite oxide nano-materials: Synthesis and applications in photocatalysis," *Materials Research Bulletin*, vol. 48, no. 10, pp. 3735-3742, 2013.

[33] A. Yaghoubi, A. Ramazani, and S. Taghavi Fardood, "Synthesis of Al_2O_3/ZrO_2 nanocomposite and the study of its effects on photocatalytic degradation of reactive blue 222 and reactive yellow 145 dyes," *ChemistrySelect*, vol. 5, no. 32, pp. 9966-9973, 2020.

[34] S. P. Keerthana, R. Yuvakkumar, P. S. Kumar, G. Ravi, and D. Velauthapillai, "Nd doped ZrO_2 photocatalyst for organic pollutants degradation in wastewater," *Environmental Technology & Innovation*, vol. 28, p. 102851, 2022.

[35] N. P. de Moraes, C. A. S. H. de Azeredo, L. A. Bacetto, M. L. C. P. da Silva, and L. A. Rodrigues, "The effect of C-doping on the properties and photocatalytic activity of ZrO_2 prepared via sol-gel route," *Optik (Stuttgart)*, vol. 165, pp. 302-309, 2018.

[36] C. V. Reddy, I. N. Reddy, K. Ravindranadh, K. R. Reddy, D. Kim, and J. Shim, "Ni-dopant concentration effect of ZrO_2 photocatalyst on photoelectrochemical water splitting and efficient removal of toxic organic pollutants," *Separation and Purification Technology.*, vol. 252, p. 117352, 2020.